

Mechanics of stretchable electronics



J. Song

Department of Engineering Mechanics and Soft Matter Research Center, Zhejiang University, Hangzhou 310027, China

ARTICLE INFO

Article history:

Received 14 October 2014

Revised 5 January 2015

Accepted 25 January 2015

Available online 9 February 2015

Keywords:

Stretchable electronics

Substrate

Film

Buckling

ABSTRACT

Recent advances in mechanics and materials provide routes to develop stretchable electronics that offer performance of conventional wafer-based devices but with the ability to be deformed to arbitrary shape. Many new applications become possible ranging from electronic eye cameras to wearable electronics, to bio-integrated therapeutic devices. This paper reviews mechanics of stretchable electronics in terms of two main forms of stretchable designs. One is wavy design, which can provide one-dimensional stretchability. The other is island-bridge design, which can be stretched in all directions. Mechanics models and their comparisons to experiments and finite element simulations are reviewed for these two designs. The results provide design guidelines for the development of stretchable electronics.

© 2015 Elsevier Ltd. All rights reserved.

1. Introduction

The vast majority of development in electronic research community has been focused on smaller and faster devices. These devices are confined to the planar surface of silicon wafers, and are hard, rigid and flat. An emerging research direction is stretchable electronics, which offers the performance of conventional wafer-based devices, but with mechanical properties of a rubber band that would enable many new applications, particularly the intimate integration of electronics with human body [1,2]. Examples include electronic eye cameras [3–5], wearable photovoltaics [6], flexible displays [7], epidermal electronics [8,9], flexible piezoelectric sensor [10], stretchable strain gauge [11], energy harvester [12], and bio-integrated therapeutic devices [13–15]. Circuits that use organic semiconductor materials can sustain large deformations [16–18], but their electrical performance is relative poor comparing with the inorganic semiconductors such as silicon, gallium arsenide, and gallium nitride. Compatibility with well developed, high performance inorganic electronic materials represents a key advantage in stretchable electronics. The main challenge is the mismatch between the soft and elastic requirements of applications and the intrinsic hard and rigid features of inorganic materials with a fracture strain $\sim 1\%$. Several mechanics strategies have been developed to make inorganic electronic materials and devices stretchable on elastomeric substrates. They can be classified into two categories.

- (1) *Wavy design*: The thin films of inorganic materials are transfer-printed to a prestretched elastomeric substrate. Releasing the prestrain leads to the formation of wavy

configuration, which can accommodate external deformations ($\sim 20\%$) through changes in wavelength and amplitude. Fig. 1 shows scanning electron micrographs of wavy design with ribbons perfectly (Fig. 1a) and partially (Fig. 1b) bonded to an elastomeric poly(dimethylsiloxane) (PDMS) substrate. This strategy has been demonstrated in different film systems such as gold [19], platinum [20], silicon nanoribbon [21,22] and nanomembranes [23], silicon nanowires [24–26], carbon nanotubes [27,28], graphene [29], and ferroelectrics [30].

- (2) *Island-bridge design*: The island-bridge mesh design is transfer-printed to a biaxially prestretched elastomeric substrate with strong chemical bonds at the locations of island (i.e., active device) and weak bonds at the locations of bridge (i.e., interconnect). The release of prestrain causes the bridge to buckle out of the plane to accommodate the deformations ($\sim 100\%$) such that the relatively rigid island experiences very small deformations. Fig. 2 shows scanning electron micrographs of island-bridge design with straight interconnects (Fig. 2a) and serpentine interconnects (Fig. 2b). The recent optimization of the bridge by using the type of fractal interconnect further increases the system stretchability [31]. This design has been widely used to various types of stretchable electronics due to the large stretchability that it can provide. Examples include electronic eye cameras [4–6], integrated circuits [32], silicon curvilinear electronics [33], LED system [34], and stretchable lithium-ion batteries [31].

Various mechanics models associated with the above designs have been developed to study the key effects on deformation modes and strain distribution. There exist several reviews of

E-mail address: jzsong@zju.edu.cn

mechanics and materials for stretchable electronics [1,2,35,36]. This article provides a brief review of the fundamental aspects of the mechanics in the wavy and island-bridge designs for stretchable electronics, through discussions of theoretical models and their quantitative comparisons to experiment. The mechanics theories for wavy design are described in Section 2 and island-bridge design in Section 3. It should be noted that the focus of island-bridge design in this article is on straight interconnects. Mechanics of serpentine or fractal interconnects is reviewed by others in this issue.

2. Mechanics of wavy design

The fabrication of stretchable wavy ribbons is illustrated in Fig. 3. The flat ribbon is transfer-printed to a prestrained compliant substrate with a perfect bond interface. When the prestrain is released, the substrate shrinks, which leads to a compression in ribbon to form the wavy layout through a nonlinear buckling response. These wavy layouts can accommodate external deformations along the ribbon direction through changes in wavelength and amplitude.

2.1. Wavy ribbon in small deformation

The thin ribbon is modeled as an elastic nonlinear von Karman beam since its thickness is much smaller comparing with other characteristic lengths (e.g., wavelength). The substrate is modeled as a semi-infinite solid because its thickness (\sim mm) is much larger than that (\sim μ m) of film. The total energy consists of the bending energy U_b and membrane energy U_m in the thin film and strain energy U_s in the substrate.

For a stiff thin film (ribbon) with thickness h_f , Young's modulus E_f and Poisson's ratio ν_f on a prestrained compliant substrate with prestrain ε_{pre} , modulus E_s , and Poisson's ratio ν_s , where $E_f \gg E_s$ (e.g., $E_f = 130$ GPa for silicon and $E_s = 1.8$ MPa for PDMS), the wavy profile forms with the out-of-plane displacement

$$w = A \cos(kx) = A \cos\left(\frac{2\pi x}{\lambda}\right), \quad (1)$$

when the prestrain is released. Here, x is the coordinate along the ribbon direction, A is the amplitude, λ is the wavelength and $k = 2\pi/\lambda$ is the wave number. The bending energy U_b can be obtained by

$$U_b = L_0 \frac{1}{\lambda} \int_0^\lambda \frac{\bar{E}_f h_f^3}{24} \left(\frac{d^2 w}{dx^2}\right)^2 dx = \frac{\pi^4 \bar{E}_f h_f^3 A^2}{3\lambda^4} L_0, \quad (2)$$

where L_0 and $\bar{E}_f = E_f/(1 - \nu_f^2)$ are the length and plane-strain modulus of thin film, respectively.

The membrane strain ε_m , which determines the membrane energy in the ribbon, is related to the in-plane displacement u and out-of-plane displacement w by $\varepsilon_m = du/dx + (dw/dx)^2/2 - \varepsilon_{pre}$. The membrane force N_m is given by $N_m = \bar{E}_f h_f \varepsilon_m$. The interfacial shear is negligible [37] and the force equilibrium then gives a constant membrane force and therefore a constant membrane strain

$$\varepsilon_m = \frac{\pi^2 A^2}{\lambda^2} - \varepsilon_{pre}, \quad (3)$$

The membrane energy U_m in the film can then be obtained by

$$U_m = L_0 \frac{1}{\lambda} \int_0^\lambda \frac{1}{2} N_m \varepsilon_m dx = \frac{1}{2} \bar{E}_f h_f \left(\frac{\pi^2 A^2}{\lambda^2} - \varepsilon_{pre}\right)^2 L_0. \quad (4)$$

The strain energy in the substrate is obtained by solving a semi-infinite solid subjected to the normal displacement in Eq. (1) and vanishing shear on its boundary as

$$U_s = \frac{\pi}{4\lambda} \bar{E}_s A^2 L_0, \quad (5)$$

where $\bar{E}_s = E_s/(1 - \nu_s^2)$ is the plane-strain modulus of the substrate.

The buckle amplitude A and wavelength λ are obtained by minimizing the total energy, i.e., $\partial(U_m + U_b + U_s)/\partial A = \partial(U_m + U_b + U_s)/\partial \lambda = 0$, as

$$\lambda = 2\pi h_f \left(\frac{\bar{E}_f}{3\bar{E}_s}\right)^{1/3}, \quad A = h_f \sqrt{\frac{\varepsilon_{pre}}{\varepsilon_c} - 1}, \quad (6)$$

where

$$\varepsilon_c = \frac{1}{4} \left(\frac{3\bar{E}_s}{\bar{E}_f}\right)^{2/3}, \quad (7)$$

is the critical strain for buckling and is extremely small (e.g., 0.034% for silicon/PDMS system). When $\varepsilon_{pre} < \varepsilon_c$, no buckling occur and the ribbon remains flat. When $\varepsilon_{pre} > \varepsilon_c$, the ribbon buckles with a constant membrane strain $\varepsilon_{membrane} = -\varepsilon_c$. The maximum bending strain is given by $\varepsilon_{bending} = 2\sqrt{(\varepsilon_{pre} - \varepsilon_c)\varepsilon_c}$. The peak strain ε_{peak} , which is the sum of membrane strain and bending strains, is approximated by

$$\varepsilon_{peak} \approx 2\sqrt{\varepsilon_{pre}\varepsilon_c}, \quad (8)$$

for small ε_c .

For the buckled system subjected to the applied strain $\varepsilon_{applied}$, the wavelength and amplitude become

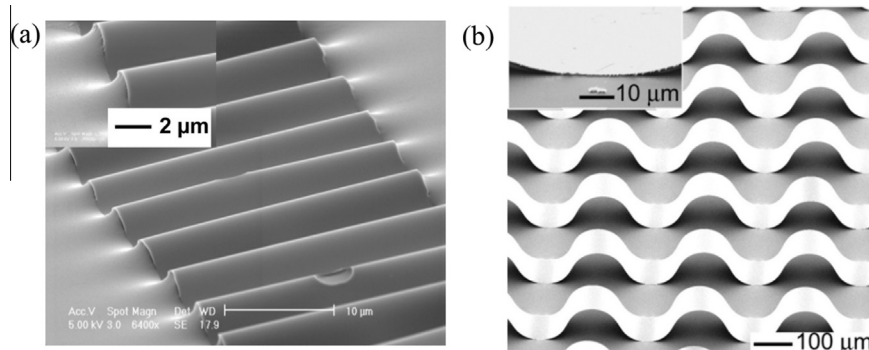


Fig. 1. Scanning electron microscope (SEM) images of wavy design with ribbon (a) perfectly and (b) partially bonded to a compliant substrate. (Reprinted with permission from Ref. [35].)

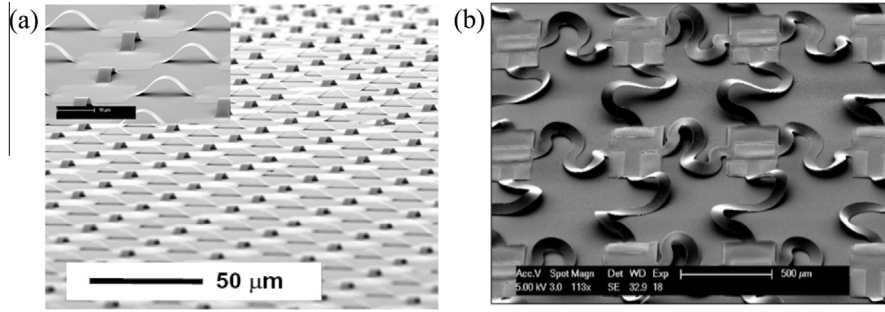


Fig. 2. Scanning electron microscope (SEM) images of island-bridge design with (a) straight and (b) serpentine interconnects. (Reprinted with permission from Ref. [35].)

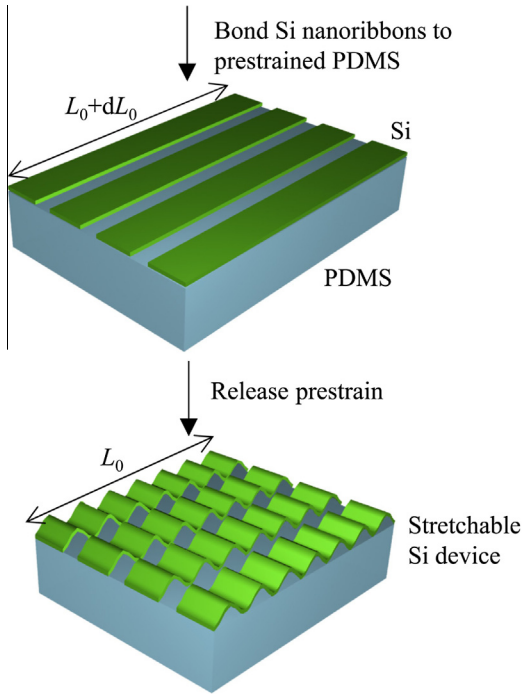


Fig. 3. Schematic illustration of the process for fabricating wavy Si ribbons on a PDMS substrate.

$$\lambda = 2\pi h_f \left(\frac{\bar{E}_f}{3\bar{E}_s} \right)^{1/3}, \quad A = h_f \sqrt{\frac{\varepsilon_{pre} - \varepsilon_{applied}}{\varepsilon_c} - 1}, \quad (9)$$

and the peak strain in the ribbon is

$$\varepsilon_{peak} \approx 2\sqrt{(\varepsilon_{pre} - \varepsilon_{applied})\varepsilon_c}. \quad (10)$$

2.2. Wavy ribbon in large deformation

The wavelengths in Eqs. (6) and (9) are constant and strain-independent, and have been widely used in high precision micro and nano-metrology methods [38]. However, when the prestrain is large, the experiments [39,40] showed that the wavelength depends on the prestrain and decreases with the increase of the prestrain. Jiang et al. [39] and Song et al. [41] showed that the strain-dependent wavelength is due to the finite deformation (i.e., large strain) in the compliant substrate, and established a finite-deformation model to understand strain-dependent wavelength by accounting for 3 factors: (1) finite geometry change (i.e., different strain-free or stress-free states for the ribbon and substrate) as shown in Fig. 4, (2) nonlinear strain-displacement

relation and (3) nonlinear constitutive model for the substrate. Cheng and Song [42] showed that the finite geometry change dominates among all three factors and their model with a consideration of finite geometry change alone simplifies the analysis significantly and is described below.

The out-of-plane displacement of the buckled thin ribbon can be represented by

$$w = A \cos\left(\frac{2\pi x}{\lambda}\right) = A \cos\left[\frac{2\pi x'}{(1 + \varepsilon_{pre})\lambda}\right], \quad (11)$$

where the coordinate x in the strain-free state for the substrate and x' in the strain-free state for the ribbon are related by $x' = (1 + \varepsilon_{pre})x$. The thin ribbon is still modeled as a von Karman beam. Using a similar approach in Section 2.1, the bending energy and membrane energy in the film can be obtained as

$$U_b = \frac{\pi^4 \bar{E}_f h_f^3 A^2}{3[(1 + \varepsilon_{pre})\lambda]^4} (1 + \varepsilon_{pre})L_0, \quad (12)$$

and

$$U_m = \frac{\bar{E}_f h_f}{2} \left[\frac{\pi^2 A^2}{(1 + \varepsilon_{pre})^2 \lambda^2} - \frac{\varepsilon_{pre}}{1 + \varepsilon_{pre}} \right]^2 (1 + \varepsilon_{pre})L_0. \quad (13)$$

where $(1 + \varepsilon_{pre})L_0$ is the original length of the ribbon. For the substrate subject to a normal displacement w and a vanishing shear stress, the substrate energy is still given by Eq. (5). Minimization of the total energy gives the wavelength and amplitude

$$\lambda = \frac{2\pi h_f}{1 + \varepsilon_{pre}} \left(\frac{\bar{E}_f}{3\bar{E}_s} \right)^{1/3}, \quad A = h_f \sqrt{\frac{\varepsilon_{pre}}{(1 + \varepsilon_{pre})\varepsilon_c} - 1}, \quad (14)$$

The peak strain in the buckled system then becomes

$$\varepsilon_{peak} \approx 2\sqrt{\frac{\varepsilon_{pre}}{1 + \varepsilon_{pre}} \varepsilon_c}. \quad (15)$$

Both wavelength and amplitude agree well with experimental data and finite element simulations without any parameter fitting as shown in Fig. 5a. A direct comparison between the predictions from Eq. (14) and finite deformation theory [41] clearly shows the finite strain and the nonlinear constitutive law lead to negligible effects on the results.

When the buckled system is subjected to the applied strain $\varepsilon_{applied}$, the out-of-plane displacement is written as

$$w = A'' \cos\left(\frac{2\pi x''}{\lambda''}\right) = A'' \cos\left[\frac{2\pi x'(1 + \varepsilon_{applied})}{\lambda''(1 + \varepsilon_{pre})}\right], \quad (16)$$

where $x'' = (1 + \varepsilon_{applied})x$ is the coordinate in the stretched state. The bending, membrane and substrate energies are then given by

$$U_b = \frac{\pi^4 \bar{E}_f h_f^3 A''^2 (1 + \varepsilon_{applied})^4}{3[(1 + \varepsilon_{pre})\lambda'']^4} (1 + \varepsilon_{pre})L_0, \quad (17)$$

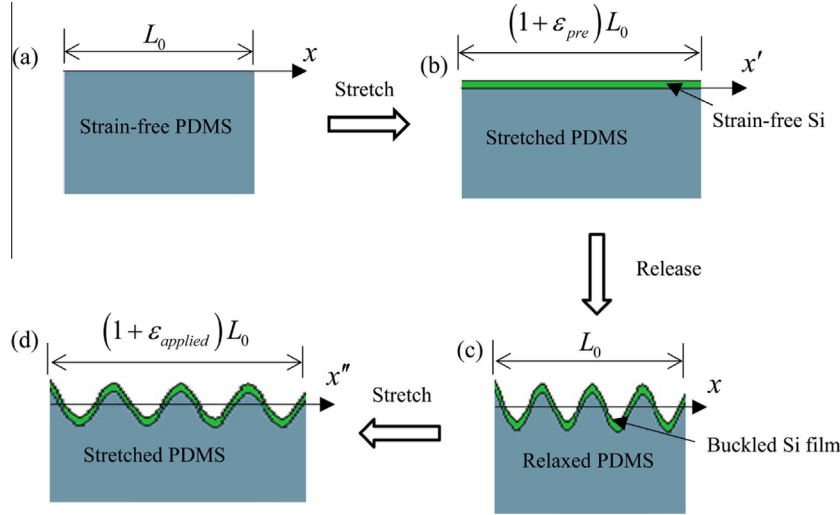


Fig. 4. The sequential configurations for the thin film/substrate buckling process. (Reprinted with permission from Ref. [41].)

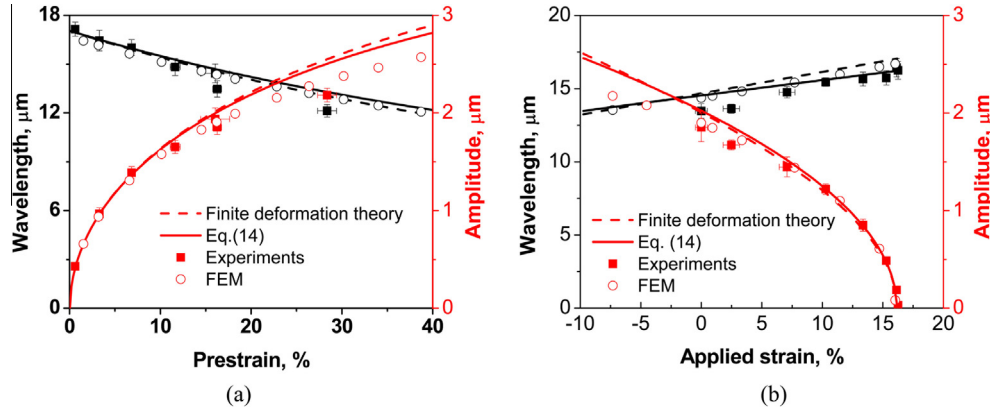


Fig. 5. Wavelength and amplitude as a function of (a) prestrain and (b) applied strain with a prestrain of 16.2%. (Reprinted with permission from Ref. [42].)

$$U_m = \frac{\bar{E}_f h_f}{2} \left[\frac{\pi^2 A'^2 (1 + \epsilon_{applied})^2}{(1 + \epsilon_{pre})^2 \lambda'^2} + \frac{\epsilon_{applied} - \epsilon_{pre}}{1 + \epsilon_{pre}} \right]^2 (1 + \epsilon_{pre}) L_0, \quad (18)$$

$$U_s = \frac{\pi}{4\lambda''} \bar{E}_s A'^2 (1 + \epsilon_{applied}) L_0. \quad (19)$$

Minimization of the total energy gives the wavelength and amplitude

$$\lambda'' = \frac{2\pi h_f (1 + \epsilon_{applied})}{1 + \epsilon_{pre}} \left(\frac{\bar{E}_f}{3\bar{E}_s} \right)^{1/3}, \quad A'' = h_f \sqrt{\frac{\epsilon_{pre} - \epsilon_{applied}}{(1 + \epsilon_{pre}) \epsilon_c}} - 1, \quad (20)$$

which agree well with experiments and finite element simulations as shown in Fig. 5b with a prestrain of 16.2%. As the tensile strain increases, the wavelength increases but the amplitude decreases. Once the tensile strain reaches the prestrain plus the critical strain, the amplitude becomes zero and further stretch $\epsilon_{fracture}$ will fracture the film. Therefore, the stretchability is given by $\epsilon_{pre} + \epsilon_{fracture} + \epsilon_c$.

The peak strain in the ribbon is given by

$$\epsilon_{peak} \approx 2 \sqrt{\frac{\epsilon_{pre} - \epsilon_{applied}}{1 + \epsilon_{pre}} \epsilon_c}. \quad (21)$$

The compressibility is the maximum applied compressive strain when the peak strain reaches $\epsilon_{fracture}$ and it is well approximated by

$$\frac{\epsilon_{fracture}^2}{4\epsilon_c} (1 + \epsilon_{pre}) - \epsilon_{pre}.$$

2.3. Wavy design with the ribbons partially bonded to the compliant substrate

Wavy design with the ribbons perfectly bonded to the compliant substrate is determined by materials properties (e.g., moduli and thickness) without any direct control over the wavy geometries. To overcome this limitation, Sun et al. [22] combined lithographically patterned surface bonding chemistry and a buckling process to develop wavy design with the ribbons partially bonded to the compliant substrate. The fabrication procedure is illustrated in Fig. 6.

The ribbon is bonded to the prestrained substrate only at certain locations. Let W_{act} denote the width of activated regions, where chemical bonding occurs between the ribbon and the substrate, and W_{in} denote the width of inactivated regions, where only weak van der Waals interactions occur at the interface as shown in Fig. 6a. Thin ribbons are then attached to the prestrained and patterned PDMS substrate (Fig. 6b) with the ribbon direction parallel to the prestretched direction. Releasing the prestrain leads to compression, which causes the ribbon on the inactivated regions to buckle and form the popup structure as shown in Fig. 6c.

Jiang et al. [43] developed an analytical model to study the buckling behavior of such systems and to predict the maximum

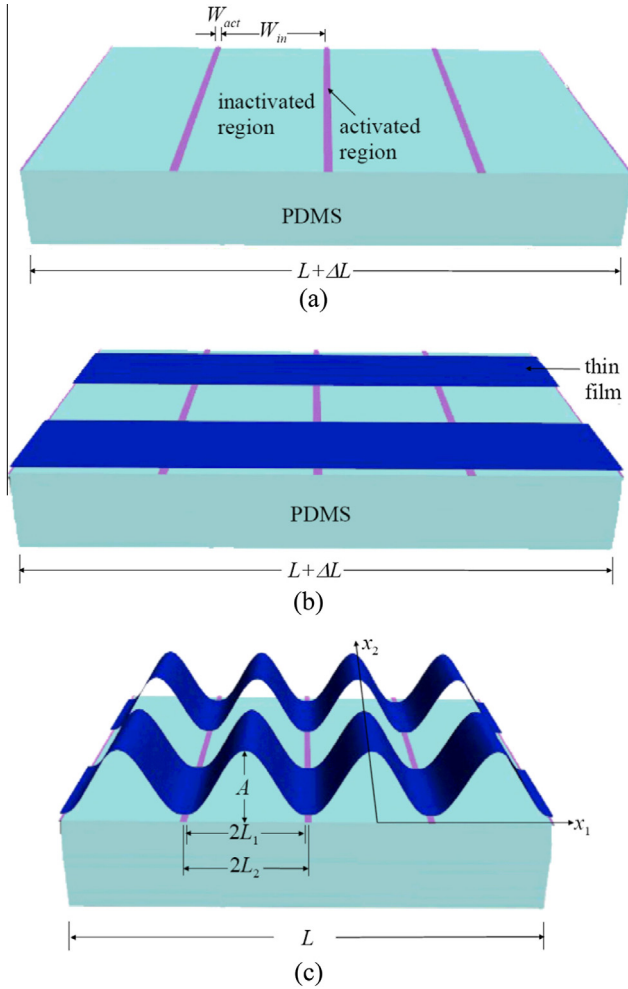


Fig. 6. (a) Prestrained PDMS with periodic activated and inactivated patterns. (b) A thin film parallel to the prestrain direction is attached to the prestrained and patterned PDMS substrate. (c) The relaxation of the prestrain ϵ_{pre} in PDMS leads to buckles of thin film.

strain in the ribbons as a function of interfacial pattern. The buckling profile of the ribbon can be expressed as

$$w = \begin{cases} w_1 = \frac{1}{2}A(1 + \cos \frac{\pi x_1}{L_1}), & -L_1 < x_1 < L_1 \\ w_2 = 0, & L_1 < |x_1| < L_2 \end{cases}, \quad (22)$$

where A is the buckling amplitude to be determined, $2L_1 = \frac{W_{in}}{1+\epsilon_{pre}}$ is the buckling wavelength, and $2L_2 = \frac{W_{in}}{1+\epsilon_{pre}} + W_{act}$ is the sum of activated and inactivated regions after relaxation (Fig. 6c). The bending and membrane energy in the thin film can be obtained as

$$U_{bending} = \int_{-L_2}^{L_2} \frac{1}{2} \bar{E}_f h_f^3 \left(\frac{d^2 w}{dx_1^2} \right)^2 dx_1 = \frac{\pi^4}{96} \frac{\bar{E}_f h_f^3 A^2}{L_1^3}, \quad (23)$$

and

$$U_{membrane} = \bar{E}_f h_f \left(\frac{\pi^2 A^2}{16L_1 L_2} - \epsilon_{pre} \right)^2 L_2. \quad (24)$$

It should be noticed that the substrate energy

$$U_{substrate} = 0, \quad (25)$$

due to zero displacements at the interface where remains intact and vanishing stress traction at the buckled portion.

Energy minimization of the total energy gives the amplitude as

$$A = \frac{4}{\pi} \sqrt{L_1 L_2 (\epsilon_{pre} - \epsilon_c)} \approx \frac{2}{\pi} \frac{\sqrt{W_{in}(W_{in} + W_{act})\epsilon_{pre}}}{1 + \epsilon_{pre}}, \quad (26)$$

where $\epsilon_c = h_f^2 \pi^2 / (12L_1^2)$ is the critical strain for buckling, which is usually a small number in most practical applications (e.g., ϵ_c is on the order of 10^{-6} for a typical wavelength $2L_1 \sim 200 \mu\text{m}$ and ribbon thickness $h_f \sim 0.1 \mu\text{m}$). The comparison of buckled profiles is shown in Fig. 7 with $W_{act} = 10 \mu\text{m}$ and $W_{in} = 190 \mu\text{m}$. Both wavelength and amplitude agree well with experiments. The peak strain in the buckled ribbon is

$$\epsilon_{peak} \approx \frac{h_f \pi}{L_1^2} \sqrt{L_1 L_2 \epsilon_{pre}}. \quad (27)$$

For a much smaller active region (i.e., $W_{act} \ll W_{in}$), the peak strain becomes $\epsilon_{peak} \approx \pi h_f \sqrt{\epsilon_{pre}} / L_1$.

3. Mechanics of island-bridge design

A different strategy, the island-bridge design, is proposed to achieve the stretchability in all directions instead of just one direction in wavy design. Lacour et al. [44] proposed a coplanar mesh design by using stretchable metal electrodes similar to Section 2 to interconnect separately fabricated active devices while Kim et al. [32] proposed a non-coplanar mesh design to significantly increase the stretchability. We will focus on the mechanics of non-coplanar mesh design in this Section. Fig. 8 schematically illustrates the fabrication of the non-coplanar mesh design on a compliant substrate. The interconnects (also called bridges) are loosely bonded to the prestrained elastomeric substrate, while active devices (also called islands) are chemically bonded. Releasing the prestrain causes the bridge to buckle and move out of the plane of the substrate to form arc-shaped structures. The buckled bridges accommodate external deformations such that the islands have small strains.

3.1. Mechanics of Island-bridge design with straight interconnects

Song et al. [45] established an analytic model for island-bridge design with straight interconnects to understand the underlying physics and to guide the design of such systems. Fig. 9 illustrates the strain-free configuration X of the bridge, and the buckled configuration x , respectively. The buckled profile can be expressed as

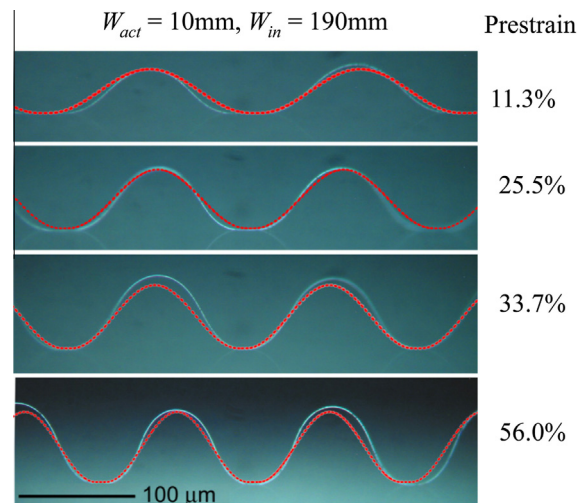


Fig. 7. Buckled GaAs thin films on patterned PDMS substrate with $W_{act} = 10 \mu\text{m}$ and $W_{in} = 190 \mu\text{m}$ for different prestrain levels, 11.3%, 25.5%, 33.7%, and 56.0% (from top to bottom). The red lines are the profiles of the buckled GaAs thin film predicted by the analytical solution. (Reprinted with permission from Ref. [43].)

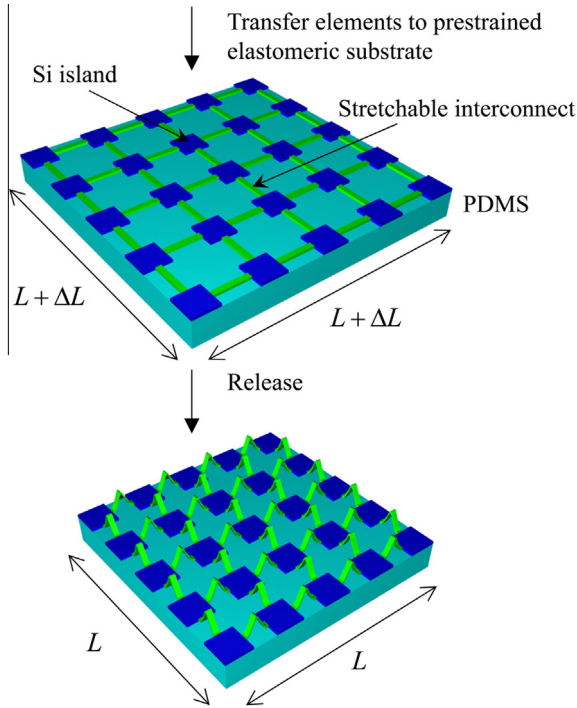


Fig. 8. Schematic illustration of the process for fabricating island-bridge design on a compliant substrate.

$$w = \frac{A}{2} \left(1 + \cos \frac{2\pi x}{L_{bridge}} \right) = \frac{A}{2} \left(1 + \cos \frac{2\pi X}{L_{bridge}^0} \right). \quad (28)$$

The total energy of the bridge consists of the bending energy

$$U_b = \frac{E_{bridge} h_{bridge}^3}{12} \frac{\pi^4 A^2}{(L_{bridge}^0)^3}, \quad (29)$$

and membrane energy

$$U_m = \frac{1}{2} E_{bridge} h_{bridge} L_{bridge}^0 \left[\frac{\pi^2 A^2}{4 (L_{bridge}^0)^2} + \frac{L_{bridge} - L_{bridge}^0}{L_{bridge}^0} \right]^2. \quad (30)$$

Minimization of total energy in the bridge gives the amplitude

$$A = \frac{2L_{bridge}^0}{\pi} \sqrt{\frac{L_{bridge}^0 - L_{bridge}}{L_{bridge}^0} - \frac{\pi^2 h_{bridge}^2}{3 (L_{bridge}^0)^2}}. \quad (31)$$

The peak strain in the bridge is

$$\epsilon_{bridge}^{max} \approx 2\pi \frac{h_{bridge}}{L_{bridge}^0} \sqrt{\frac{L_{bridge}^0 - L_{bridge}}{L_{bridge}^0}}. \quad (32)$$

Once the prestrain is relaxed, the bridge length is reduced from L_{bridge}^0 to L_{bridge} , which gives the prestrain $\epsilon_{pre} = \frac{L_{bridge}^0 - L_{bridge}}{L_{bridge}^0}$. The maximum strain in the interconnect in Eq. (32) then becomes

$$\epsilon_{bridge}^{max} = 2\pi \frac{h_{bridge}}{L_{bridge}^0} \sqrt{\frac{\epsilon_{pre}}{1 + \epsilon_{pre}}}. \quad (33)$$

For the interconnect with $L_{bridge}^0 = 20 \mu\text{m}$, $h_{bridge} = 50 \text{ nm}$ and $L_{bridge} = 17.5 \mu\text{m}$ in experiments, the analytical prediction of the amplitude is $A = 4.50 \mu\text{m}$, which agrees well with the experimentally measured value $4.76 \mu\text{m}$.

The finite element method is used to study the silicon island ($L_{island}^0 \times L_{island}^0$) on a PDMS substrate [$(L_{island}^0 + L_{bridge}) \times (L_{island}^0 + L_{bridge})$]. The island is modeled as a plate since its thickness h_{island} is much smaller than the length L_{island}^0 . The PDMS is modeled as a 3D solid, with periodic conditions on the lateral surfaces (X-Z and Y-Z planes). The displacements are continuous across the island/substrate interface, and the rest of the top surface is traction free. The buckled interconnects give the axial force $N = E_{bridge} h_{bridge} \epsilon_c$ and bending moment $M = \frac{E_{bridge} h_{bridge}^3}{12} \frac{2\pi^2 A}{(L_{bridge}^0)^2} \approx \frac{\pi E_{bridge} h_{bridge}^3}{3 L_{bridge}^0} \sqrt{\frac{\epsilon_{pre}}{1 + \epsilon_{pre}}}$ over the width w_{bridge} on each edge of the island. It is shown that the strain due to the axial force N is negligible comparing to that due to the bending moment M [45]. Combining the dimensional analysis, the peak strain in the island can be approximated by

$$\epsilon_{island}^{max} \approx 2\pi \frac{(1 - \nu_{island}^2) E_{bridge} h_{bridge}^3}{E_{island} h_{island}^2 L_{bridge}^0} \sqrt{\frac{\epsilon_{pre}}{1 + \epsilon_{pre}}}, \quad (34)$$

which clearly shows stiff and thick island reduces its strain.

In order to increase the accuracy of the analytical model in large deformation, Chen et al. [46] and Li et al. [47] improved the above model by discarding the sinusoidal assumption for the buckled interconnects.

3.2. Lateral buckling of straight interconnects

When shear or diagonal stretch (45° from the interconnects) is applied (Fig. 10), the interconnects may undergo lateral buckling. Different from Euler buckling where the displacement takes the simple sinusoidal form, lateral buckling involves large torsion and out-of-plane bending with very complex form of displacements. Most of existing results on lateral buckling, however, are based on numerical methods and closed-form solutions only exist for initial buckling but not for postbuckling. Su et al. [48] established a systematic method based on the nonlinear equilibrium equations for postbuckling of beams that may involve rather complex buckling modes such as lateral buckling. The perturbation method is used to obtain the amplitude of buckled interconnects. Chen et al. [49] derived analytical solutions for lateral buckling (initial buckling and postbuckling) of interconnects under shear. The initial buckling of interconnects is investigated through the

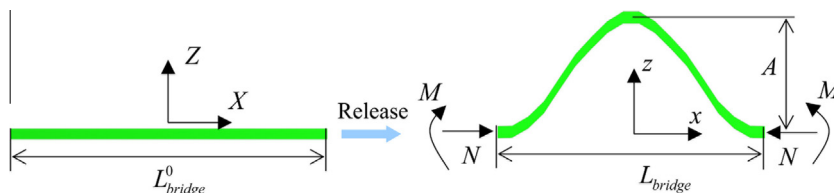


Fig. 9. Schematic diagram of mechanics model for the interconnect in an island-bridge design.

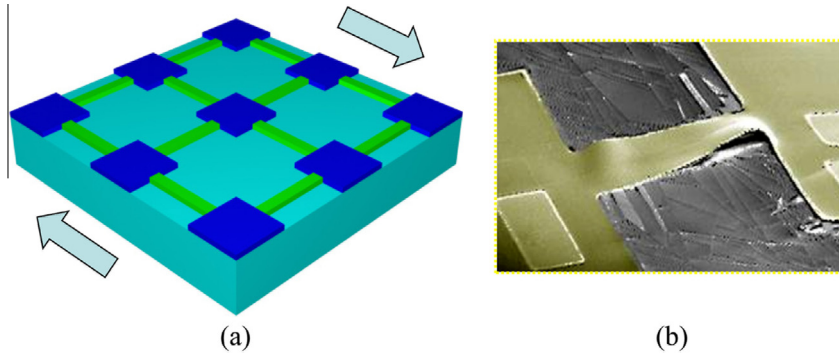


Fig. 10. (a) The schematic diagram of island-bridge design under shear; (b) SEM image of the island-bridge design under shear. (Reprinted with permission from Ref. [49].)

equilibrium equations while the postbuckling behavior is studied by energy minimization of the potential energy including up to 4th power of the displacement.

The interconnect is modeled as an L -long beam with a thin rectangular cross section $a \times b$, where $b \gg a$. The left end is fixed, and the right end is subjected to a shear or vertical displacement v_0 with no rotations (Fig. 11). The coordinates (x, y, z) is fixed in space with the axis z coinciding with the centroidal axis of the undeformed beam, and the x and y coinciding with the principal axes of the cross section. The coordinates (ξ, η, ζ) is fixed to a point on the centroidal axis of the beam and moves with it with the axes ξ and η the principal axes of the cross section on the deformed beam, and ζ coincides with the tangent to the deformed centroidal axis of the beam. The deformation of the beam is defined by the components u, v and w of the displacement of the center in the x, y and z directions and by the rotation ϕ of the cross section with the positive direction about the z axis according to the right-hand rule (Fig. 11).

By introducing a non-dimensional coordinate $s = 2z/L$ where $-1 \leq s \leq 1$, the equilibrium equations are given by

$$\begin{cases} EI_\xi \frac{d^2 v}{ds^2} = -\left(\frac{L}{2}\right)^3 p_y s \\ EI_\eta \frac{d^2 u}{ds^2} = \left(\frac{L}{2}\right)^3 [-p_y s \phi + \frac{2}{L} m_y + p_x(1-s)] \\ C \frac{d\phi}{ds} = \frac{L}{2} [p_y s \frac{du}{ds} + \frac{dv}{ds} p_x(1-s) + t - p_y u + p_x v] \end{cases}, \quad (35)$$

where $C = Ea^3b/[6(1+\nu)]$ is the torsional rigidity, E is the Young's modulus, and ν is the Poisson's ratio, $I_\xi = ab^3/12$ and $I_\eta = a^3b/12$ are the moment of inertia about axes ξ and η , respectively, p_y denotes the load in the y direction to cause v_0 on the right end, p_x the load in the x direction on the right end, m_y the bending moment in the y direction on the right end, and t the torque in the z direction on the right end. The following orders of forces and displacement hold during buckling: the applied force and displacement (i.e., p_y and v) are zero order, while the corresponding force, moment and displacement (i.e., p_x, m_y, t, u and ϕ) resulting from lateral buckling are first order. The boundary conditions are given by

$$\begin{cases} u(-1) = u'(-1) = u(1) = u'(1) = 0 \\ v(-1) = v'(-1) = v(1) = 0 \quad v(1) = v_0. \\ \phi(-1) = \phi(1) = 0 \end{cases} \quad (36)$$

After eliminating u from the second and third equations in Eq. (36) and applying $I_\xi \gg I_\eta$, we obtain

$$\frac{d^2 \phi}{ds^2} + \frac{p_y^2}{CEI_\eta} \left(\frac{L}{2}\right)^4 s^2 \phi = \left(\frac{L}{2}\right)^4 \frac{p_y}{CEI_\eta} s \left[\frac{2}{L} m_y + p_x(1-s) \right]. \quad (37)$$

The solution ϕ of Eq. (37) is either symmetric or anti-symmetric.

The symmetric buckling mode corresponds to an even function for ϕ and an odd function for u , which are obtained as

$$\phi(s) = A\bar{\phi}(s), \quad u(s) = -A\frac{L}{4}\sqrt{\frac{1}{2(1+\nu)}}\bar{u}(s), \quad (38)$$

with

$$\begin{aligned} \bar{\phi}(s) &= \sqrt[4]{s^2} J_{-1/4}\left(\frac{\alpha}{8}s^2\right) - J_{-1/4}\left(\frac{\alpha}{8}\right), \quad \text{and} \\ \bar{u}(s) &= \alpha \int_{\zeta=-1}^s \left[\int_{\xi=-1}^{\zeta} \xi \sqrt{\xi^2} J_{-1/4}\left(\frac{\alpha}{8}\xi^2\right) d\xi \right] d\zeta, \end{aligned} \quad (39)$$

A is the amplitude, J is the Bessel function and α is to be determined by $J_{3/4}(\frac{\alpha}{8}) = 0$.

The anti-symmetric buckling mode corresponds to an odd function for ϕ and an even function for u . Eq. (38) still holds but

$$\bar{\phi}(s) = \sqrt{s} J_{1/4}\left(\frac{\alpha}{8}s^2\right) + \frac{4\left(\frac{\alpha}{8}\right)^2 \int_{s=0}^1 s \sqrt{s} J_{1/4}\left(\frac{\alpha}{8}s^2\right) ds}{1 - 4\left(\frac{\alpha}{8}\right)^2 \int_{s=0}^1 s^4 \phi_p\left(\frac{\alpha}{8}s^2\right) ds} s^3 \phi_p\left(\frac{\alpha}{8}s^2\right), \quad (40)$$

and

$$\begin{aligned} \bar{u}(s) &= \alpha \int_{\zeta=-1}^s \\ &\times \int_{\xi=0}^{\zeta} \left\{ \xi \sqrt{\xi} J_{1/4}\left(\frac{\alpha}{8}\xi^2\right) - \frac{\left[1 - \frac{\alpha^2}{16}\xi^4 \phi_p\left(\frac{\alpha}{8}\xi^2\right)\right] \int_0^1 \gamma \sqrt{\gamma} J_{1/4}\left(\frac{\alpha}{8}\gamma^2\right) d\gamma}{1 - \frac{\alpha^2}{16} \int_0^1 \gamma^4 \phi_p\left(\frac{\alpha}{8}\gamma^2\right) d\gamma} \right\} d\xi d\zeta. \end{aligned} \quad (41)$$

with α satisfying

$$J_{1/4}\left(\frac{\alpha}{8}\right) + \frac{4\left(\frac{\alpha}{8}\right)^2 \int_{s=0}^1 s \sqrt{s} J_{1/4}\left(\frac{\alpha}{8}s^2\right) ds}{1 - 4\left(\frac{\alpha}{8}\right)^2 \int_{s=0}^1 s^4 \phi_p\left(\frac{\alpha}{8}s^2\right) ds} \phi_p\left(\frac{\alpha}{8}\right) = 0, \quad (42)$$

where $\phi_p(x)$ is

$$\phi_p(x) = -\frac{1}{48x^2} \left\{ \begin{aligned} &82^{3/4} x^{9/4} F_2(3/4, 5/4, 7/4; -x^2/4) J_{-1/4}(x) \Gamma(3/4) \\ &-6\sqrt{2}\pi x^2 J_{1/4}(x) J_{-1/4}(x) + 3\sqrt{2}\pi x^{7/4} J_{1/4}(x) J_{3/4}(x) S_{1/4,7/4}(x) \\ &-9\sqrt{2}\pi x^{3/4} J_{1/4}(x) J_{3/4}(x) S_{5/4,3/4}(x) + 6\sqrt{2}\pi x^{7/4} J_{1/4}(x) J_{-1/4}(x) S_{5/4,3/4}(x) \end{aligned} \right\}. \quad (43)$$

F is the hypergeometric function, Γ is the gamma function, and S is the Lommel function.

The critical load for lateral buckling is then given by $p_y^{cr} = \frac{Ea^3b}{6L^2} \sqrt{\frac{1}{2(1+\nu)}} \alpha$, which gives the critical displacement as

$$v_0^{cr} = \frac{La^2\alpha}{6b^2} \sqrt{\frac{1}{2(1+\nu)}}. \quad (44)$$

Energy method is used to study the postbuckling behavior of interconnects. The displacements due to buckling at neutral axis are $u(z), v(z)$ and $w(z)$. Then the general point at a section has the following displacements by ignoring the warping as

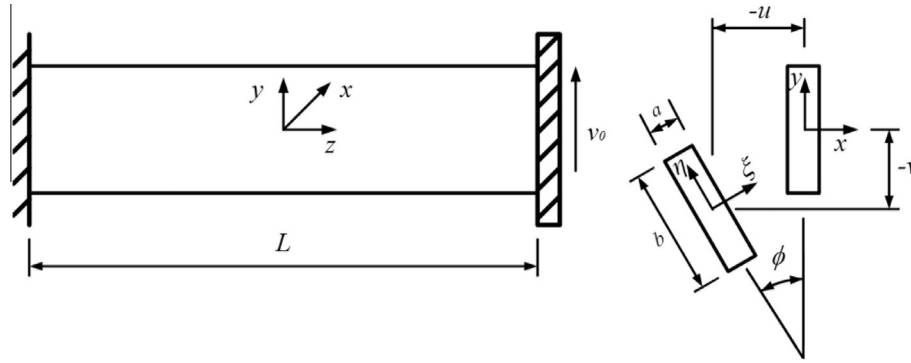


Fig. 11. The schematic diagram of lateral buckling of a beam.

$$\begin{cases} u_1(x, y, z) = u(z) - \phi(z)y \\ v_1(x, y, z) = v(z) + \phi(z)x \\ w_1(x, y, z) = w(z) - u'(z)x - v'(z)y \end{cases} \quad (45)$$

The longitudinal and shear strains due to buckling can be calculated by

$$\begin{cases} \epsilon_{zz} = \frac{\partial w_1}{\partial z} + \frac{1}{2} \left(\frac{\partial u_1}{\partial z} \right)^2 + \frac{1}{2} \left(\frac{\partial v_1}{\partial z} \right)^2 + \frac{1}{2} \left(\frac{\partial w_1}{\partial z} \right)^2 \\ \epsilon_{yz} = \frac{1}{2} \left(\frac{\partial v_1}{\partial z} + \frac{\partial w_1}{\partial y} + \frac{\partial u_1}{\partial y} \frac{\partial u_1}{\partial z} + \frac{\partial v_1}{\partial y} \frac{\partial v_1}{\partial z} + \frac{\partial w_1}{\partial y} \frac{\partial w_1}{\partial z} \right) \end{cases} \quad (46)$$

The strain energy of the beam can be obtained by

$$U_{strain} = \int_V \left[\sigma_z^0 \epsilon_{zz} + \frac{1}{2} E \epsilon_{zz}^2 + \sigma_{yz}^0 2 \epsilon_{yz} \right] dV + \frac{1}{2} C \int_{z=0}^L \left(\frac{d\phi}{dz} \right)^2 dz, \quad (47)$$

where $\sigma_z^0 = p_y y z / I_z$ is the initial normal stress in the cross section due to bending, $\sigma_{yz}^0 = p_y / (ab)$ is the initial shear stress, $p_y = \frac{E a^3 b}{6 L^2} \sqrt{\frac{1}{2(1+\nu)}} \alpha$, C is the torsional rigidity, and V is the volume of the beam. The force equilibrium in z direction $\int_A E \epsilon_{zz} dA = 0$ yields $w' = -\frac{1}{2} u'^2 - \frac{1}{24} \phi'^2 (a^2 + b^2)$. The energy then becomes

$$U_{strain} = A^2 \frac{E a^3 b}{96(1+\nu)L} \left[-\frac{24 \alpha b^2 v_0}{a^2 L} \sqrt{\frac{1+\nu}{2}} (C_1 + C_5) + 16 C_6 + \alpha^2 C_3 \right] + A^4 \frac{E a b^5}{8 L^3} \left\{ \frac{7}{45} C_2 + \frac{\alpha^2 L^2}{12(1+\nu)b^2} C_4 \right\}, \quad (48)$$

where C_1 – C_6 are constants, which only depend on the buckling shapes and are given by

$$\begin{aligned} C_1 &= \int_{s=-1}^1 s \bar{u}'(s) \bar{\phi}'(s) ds, & C_2 &= \int_{s=-1}^1 \bar{\phi}'(s)^4 ds, & C_3 &= \int_{s=-1}^1 \bar{u}''(s)^2 ds, \\ C_4 &= \int_{s=-1}^1 \bar{u}'(s)^2 \bar{\phi}'(s)^2 ds, & C_5 &= \int_{s=-1}^1 \bar{\phi}(s) \bar{u}'(s) ds, & C_6 &= \int_{s=-1}^1 \bar{\phi}'(s)^2 ds. \end{aligned} \quad (49)$$

Minimization of the energy yields

$$A = \frac{1}{\sqrt{L}} \sqrt{\frac{\alpha(C_1 + C_5)}{\sqrt{2} \left(\frac{7C_2}{45} \frac{b^2}{L^2} + \frac{\alpha^2 C_4}{12(1+\nu)} \right) \sqrt{1+\nu}}} \cdot \sqrt{v_0 - \frac{16C_6 + \alpha^2 C_3}{12\sqrt{2}(C_1 + C_5)\alpha} \frac{a^2 L}{b^2 \sqrt{1+\nu}}}. \quad (50)$$

We take a beam with $L = 20$, $a = 1$, $b = 0.1$, and $\nu = 0.3$ as an example to show our results. The critical displacements $v_0^c = 0.5773$ and 1.1002 from Eq. (44) for the first and second symmetrical buckling modes agree very well with finite element simulations 0.5613 and 1.0708 . The critical displacement $v_0^c = 0.7632$ and 1.0001 for the first and second anti-symmetrical buckling modes also agree well with finite element simulations 0.7620 and 0.9732 . According to the magnitude of critical displacement, mode 1 for lateral buckling is symmetric, mode 2 is anti-symmetric, mode 3 is anti-symmetric and mode 4 is symmetric. The buckling shapes of rotation of the cross section and

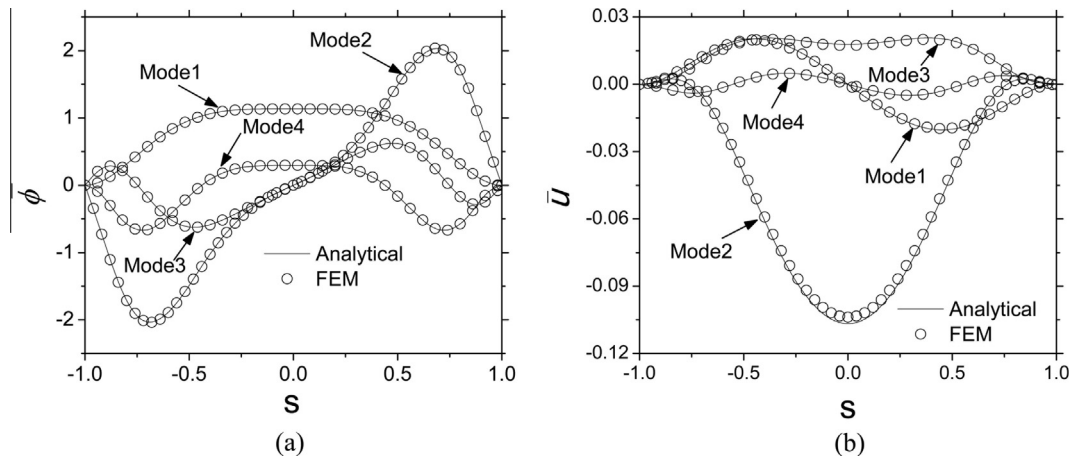


Fig. 12. The buckling shape of (a) rotation of the cross section $\bar{\phi}(s)$ and (b) displacement of center in x direction $\bar{u}(s)$. (Reprinted with permission from Ref. [49].)

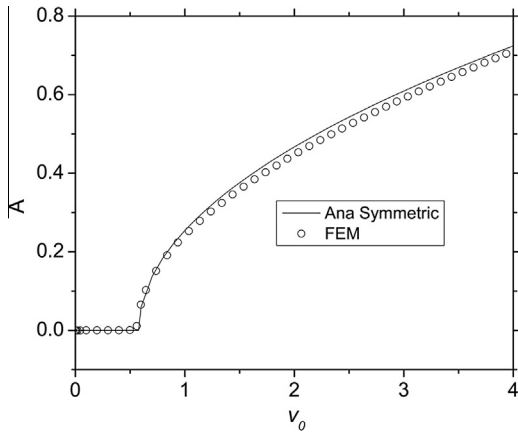


Fig. 13. The amplitude A versus the applied displacement v_0 for the buckling mode 1 of a beam with $L = 20$, $a = 1$, $b = 0.1$, and $\nu = 0.3$. (Reprinted with permission from Ref. [49].)

displacement of center in x direction, $\bar{\phi}(s)$ and $\bar{u}(s)$, are shown in Fig. 12 and they have a very good agreement between the analytical predictions and finite element simulations.

Let's consider the postbuckling for mode 1 with $\alpha = 27.9280$. The amplitude A in Eq. (50) then becomes

$$A = \frac{1.3336}{\sqrt{L}} \sqrt{\frac{1}{(3.4001 \frac{b^2}{L^2} + \frac{0.6584}{1+\nu}) \sqrt{1+\nu}}} \cdot \sqrt{v_0 - 3.2905 \frac{a^2 L}{b^2 \sqrt{1+\nu}}} \quad (51)$$

For $b \ll L$, if $b \ll L$, A can be simplified as

$$A = 1.6435 \sqrt[4]{1+\nu} \cdot \sqrt{\frac{v_0}{L} - 3.2905 \frac{1}{\sqrt{1+\nu}} \frac{a^2}{b^2}} \quad (52)$$

Fig. 13 shows the amplitude A versus the applied displacement v_0 for the buckling mode 1. The amplitude A remains zero when v_0 is smaller than a critical value, $v_0^{cr} = 0.5773$, and buckling does not occur. Once v_0 exceeds the critical value, lateral buckling occurs and the amplitude increases as v_0 increases. As shown in Fig. 13, the finite element results agree well with analytical solutions.

3.3. Buckling of serpentine interconnects

To expand the stretchability even further, serpentine interconnects can be used as shown in Fig. 2b. The serpentine interconnects have two major advantages over straight ones: (1) they are much longer than straight interconnects, and therefore can accommodate much larger prestrain; (2) once the applied strain reaches the prestrain, straight interconnects become flat and lose their stretchability, but serpentine interconnects can be stretched much further because large twist will be involved to accommodate the larger deformation.

Due to the complex geometry, analytical models to investigate the deformation of serpentine interconnects are very limited [50]. Finite element simulations have been widely used for the buckling of serpentine interconnects. Fig. 14 shows the strain distribution in a CMOS inverter before (35% prestrain) and after (70% applied strain) stretching with serpentine interconnects consisting of polyimide and metal layers and islands consisting of polyimide, SiO_2 , Si and metal layers [32]. It is shown that the peak strain in the metal layer of interconnects and islands are lower than 2% even for the stretch to 70%.

3.4. Buckling of fractal interconnects

Recently, fractal interconnects are proposed as a route to achieve both large system-level stretchability and high areal coverage of device islands [31]. Fig. 15 shows an example of interconnect in Hilbert fractal design up to a level-5 iteration. The level-1 pattern has a U shape, and higher levels correspond to self-similar assemblies of the patterns in the previous levels. For each level

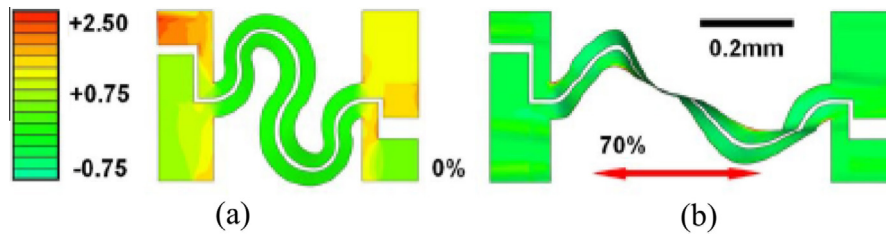


Fig. 14. Strain distribution in metal layer of CMOS inverter (a) before (35% prestrain) and (b) after (70% applied strain) stretching. (Reprinted with permission from Ref. [32].)

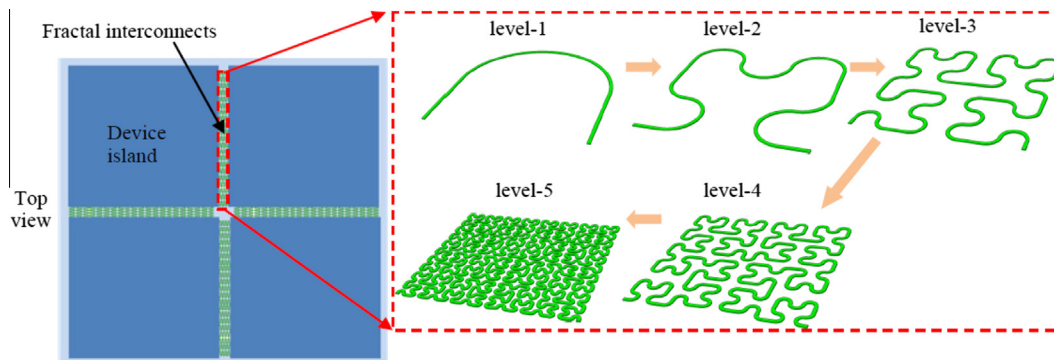


Fig. 15. Schematic diagram of island-bridge design with fractal interconnects.

increase, the total length of fractal interconnects increases approximately by a factor of 2 for fixed spacing between device islands. This scaling leads to large stretchability in the interconnects, and therefore large system-level stretchability. It is shown that the interconnect buckles (therefore loses its tensile rigidity) to accommodate the large stretch, in a mechanism of “unraveling” of the fractal interconnect that begins at the highest level interconnect and propagates to lower levels. This mechanism is fully reversible, i.e., resuming to the fractal pattern upon unloading if the fractal interconnects do not reach plastic yielding. Mechanics of fractal interconnects is reviewed by others in this issue and we will not explore more.

4. Conclusion

We have reviewed the mechanics of wavy design and island-bridge design for stretchable electronics. Both the buckling geometry (wavelength and amplitude) and the peak strains are obtained analytically. The solutions agree well with experiments and/or finite element simulations, and clearly show how the buckled profile reduces the strain to achieve the large stretchability.

Wavy design: For the ribbon perfectly bonded to the compliant substrate, both small-deformation and simplified finite-deformation analyses are performed. The simplified finite-deformation model predicts a strain-dependent wavelength while small-deformation one gives a strain-independent wavelength. For the ribbon partially bonded to the compliant substrate, the portion of the ribbon without bonding to the substrate delaminates from the substrate to form the pop up structure when the prestrain is released. The wavelength and amplitude depend on the geometry and can be precisely controlled to lower the peak strain to a larger stretchability.

Island-bridge design: An analytical model is established for island-bridge design with straight interconnects. The results predict analytically the buckling amplitude, which agrees well with experiments without any parameter fitting. The peak strains in the interconnects and islands are also obtained analytically. Analytical models are established to study the lateral buckling of straight interconnects under shear. Analytical expressions are obtained for the critical load and buckling shape at the onset of buckling by solving the equilibrium equations. The postbuckling behavior is studied by energy minimization of the potential energy including up to fourth power of the displacement. A simple expression of the amplitude characterizing the deformation after buckling is obtained. Finite element models are developed to study the buckling behavior of island-bridge design with serpentine interconnects. Mechanics of fractal interconnects are also discussed.

The two different designs have their own pros and cons. Wavy design is able to provide a high areal coverage of active devices since they can be integrated directly on the wavy film. However, wavy design can only offer large stretchability ($\sim 100\%$) in one direction or small stretchability $\sim 10\%$ in all directions [23,51]. Island-bridge design is able to provide large stretchability ($>100\%$) in all directions. However, because only islands serve as active devices in island-bridge design, the areal coverage of the active devices is usually low unless using a serpentine or fractal bridge. These results are helpful to future designers of stretchable electronics to make selections between the two stretchable strategies.

Acknowledgements

J.S. acknowledges the supports from the National Natural Science Foundation of China (Grant Nos. 11372272 and

11321202), the National Basic Research Program of China (Grant No. 2015CB351900), and the Thousand Young Talents Program of China.

References

- [1] Rogers JA, Someya T, Huang Y. Materials and mechanics for stretchable electronics. *Science* 2010;327:1603–7.
- [2] Kim DH, Ghaffari R, Lu N, Rogers JA. Flexible and stretchable electronics for biointegrated devices. *Annu Rev Biomed Eng* 2012;14:113–28.
- [3] Ko HC, Stoykovich MP, Song J, Malyarchuk V, Choi WM, Yu CJ, et al. A hemispherical electronic eye camera based on compressible silicon optoelectronics. *Nature* 2008;454:748–53.
- [4] Jung I, Xiao J, Malyarchuk V, Lu C, Li M, Liu Z, et al. Dynamically tunable hemispherical electronic eye camera system with adjustable zoom capability. *Proc Natl Acad Sci USA* 2011;108:1788–93.
- [5] Song YM, Xie Y, Malyarchuk V, Xiao J, Jung I, Choi KJ, et al. Digital cameras with designs inspired by the arthropod eye. *Nature* 2013;497:95–9.
- [6] Yoon J, Baca AJ, Park SI, Elvikis P, Geddes JB, Li L, et al. Ultrathin silicon solar microcells for semitransparent, mechanically flexible and microconcentrator module designs. *Nat Mater* 2008;7:907–15.
- [7] Crawford GP. Flexible flat panel display technology. New York: Wiley; 2005.
- [8] Kim DH, Lu N, Ma R, Kim YS, Kim RH, Wang S, et al. Epidermal electronics. *Science* 2011;333:838–43.
- [9] Webb RC, Bonifas AP, Behnaz A, Zhang Y, Yu KJ, Cheng H, et al. Ultrathin conformal devices for precise and continuous thermal characterization of human skin. *Nat Mater* 2013;12:938–44.
- [10] Persano L, Dagdeviren C, Su Y, Zhang Y, Girardo S, Pisignano D, et al. High performance piezoelectric devices based on aligned arrays of nanofibers of poly(vinylidene fluoride-co-trifluoroethylene). *Nat Commun* 2013;4:1633.
- [11] Yang S, Lu N. Gauge factor and stretchability of silicon-on-polymer strain gauges. *Sensors* 2013;13:8577–94.
- [12] Dagdeviren C, Hwang SW, Su Y, Kim S, Cheng H, Gur O, et al. Transient, biocompatible electronics and energy harvesters based on ZnO. *Small* 2013;9:3398–404.
- [13] Kim DH, Viventi J, Amsden JJ, Xiao J, Vigeland L, Kim YS, et al. Dissolvable films of silk fibroin for ultrathin conformal bio-integrated electronics. *Nat Mater* 2010;9:511–7.
- [14] Kim DH, Lu N, Ghaffari R, Kim YS, Lee SP, Xu L, et al. Materials for multifunctional balloon catheters with capabilities in cardiac electrophysiological mapping and ablation therapy. *Nat Mater* 2011;10:316–23.
- [15] Viventi J, Kim DH, Vigeland L, Frechette ES, Blanco JA, Kim YS, et al. Flexible, foldable, actively multiplexed, high-density electrode array for mapping brain activity in vivo. *Nat Neurosci* 2011;14:1599–605.
- [16] Garnier F. Thin-film transistors based on organic conjugated semiconductors. *Chem Phys* 1998;227:253–62.
- [17] Crone B et al. Large-scale complementary integrated circuits based on organic transistors. *Nature* 2000;403:521–3.
- [18] Loo YL, Someya T, Baldwin KW, Bao ZN, Ho P, Dodabalapur A, et al. Soft, conformable electrical contacts for organic semiconductor: high-resolution plastic circuits by lamination. *Proc Natl Acad Sci USA* 2002;99:10252–6.
- [19] Bowden N, Brittain S, Evans AG, Hutchinson JW, Whitesides GM. Spontaneous formation of ordered structures in thin films of metals supported on an elastomeric polymer. *Nature* 1998;393:146–9.
- [20] Ohzono T, Matsushita SI, Shimomura M. Coupling of wrinkle patterns to microsphere-array lithographic patterns. *Soft Matter* 2005;1:227–30.
- [21] Khang D, Jiang H, Huang Y, Rogers JA. A stretchable form of single-crystal silicon for high-performance electronics on rubber substrates. *Science* 2006;311:208–12.
- [22] Sun Y, Choi WM, Jiang H, Huang Y, Rogers JA. Controlled buckling of semiconductor nanoribbons for stretchable electronics. *Nat Nanotechnol* 2006;1:201–7.
- [23] Choi WM, Song J, Khang D, Jiang H, Huang Y, Rogers JA. Biaxially stretchable “wavy” silicon nanomembranes. *Nano Lett* 2007;7:1655–63.
- [24] Baca AJ, Ahn JH, Sun Y, Meitl MA, Menard E, Kim HS, et al. Semiconductor wires and ribbons for high-performance flexible electronics. *Angew Chem Int Ed* 2008;47:5524–42.
- [25] Ryu SY, Xiao J, Park WI, Son KS, Huang Y, Paik U, et al. Lateral buckling mechanics in silicon nanowires on elastomeric substrates. *Nano Lett* 2009;9:3214–9.
- [26] Xiao J, Ryu SY, Huang Y, Hwang KC, Paik U, Rogers JA. Mechanics of nanowire/nanotube in-surface buckling on elastomeric substrates. *Nanotechnology* 2010;21:85708.
- [27] Khang D, Xiao J, Kocbas C, MacLaren S, Banks T, Jiang H, et al. Molecular scale buckling mechanics in individual aligned single-wall carbon nanotubes on elastomeric substrates. *Nano Lett* 2008;8:124–30.
- [28] Xiao J, Jiang H, Khang D, Wu J, Huang Y, Rogers JA. Mechanics of buckled carbon nanotubes on elastomeric substrates. *J Appl Phys* 2008;104:033543.
- [29] Kim RH, Bae MH, Kim DG, Cheng H, Kim BH, Kim DH, et al. Stretchable, transparent graphene interconnects for arrays of microscale inorganic light emitting diodes on rubber substrates. *Nano Lett* 2011;11(9):3881–6.
- [30] Feng X, Yang BD, Liu Y, Wang Y, Dagdeviren C, Liu Z, et al. Stretchable ferroelectric nanoribbons with wavy configurations on elastomeric substrates. *ACS Nano* 2011;5:3326–32.

- [31] Xu S, Zhang Y, Cho J, Lee J, Huang X, Jia L, et al. Stretchable batteries with self-similar serpentine interconnects and integrated wireless recharging systems. *Nat Commun* 2013;4:1543.
- [32] Kim DH, Song J, Choi WM, Kim HS, Kim RH, Liu Z, et al. Materials and noncoplanar mesh designs for integrated circuits with linear elastic responses to extreme mechanical deformations. *Proc Natl Acad Sci USA* 2008;105:18675–80.
- [33] Ko HC, Shin G, Wang S, Stoykovich MP, Lee JW, Kim DH, et al. Curvilinear electronics formed using silicon membrane circuits and elastomeric transfer elements. *Small* 2009;5:2703–9.
- [34] Park SI, Xiong Y, Kim RH, Elvikis P, Meitl M, Kim DH, et al. Printed assemblies of inorganic light-emitting diodes for deformable and semitransparent displays. *Science* 2009;325:977–81.
- [35] Song J, Jiang H, Huang Y, Rogers JA. Mechanics of stretchable inorganic electronic materials. *J Vac Sci Technol A* 2009;27:1107–25.
- [36] Kim DH, Xiao J, Song J, Huang Y, Rogers JA. Stretchable, curvilinear electronics based on inorganic materials. *Adv Mater* 2010;22:1–17.
- [37] Huang ZY, Hong W, Suo Z. Nonlinear analyses of wrinkles in a film bonded to a compliant substrate. *J Mech Phys Solids* 2005;53:2101–18.
- [38] Stafford CM, Vogt BD, Harrison C, Julthongpipit D, Huang R. Elastic moduli of ultrathin amorphous polymer films. *Macromolecules* 2006;39:5095–9.
- [39] Jiang H, Khang DY, Song J, Sun Y, Huang Y, Rogers JA. Finite deformation mechanics in buckled thin films on compliant supports. *Proc Natl Acad Sci USA* 2007;104:15607–12.
- [40] Harrison C, Stafford CM, Zhang WH, Karim A. Sinusoidal phase grating created by tunably buckled surface. *Appl Phys Lett* 2004;85:4016–8.
- [41] Song J, Jiang H, Liu Z, Khang DY, Huang Y, Rogers JA, et al. Buckling of a stiff thin film on a compliant substrate in large deformation. *Int J Solids Struct* 2008;45:3107–21.
- [42] Cheng H, Song J. A simply analytic study of buckled thin films on compliant substrates. *ASME J Appl Mech* 2013;81:024501.
- [43] Jiang H, Sun Y, Rogers JA, Huang Y. Mechanics of precisely controlled thin film buckling on elastomeric substrate. *Appl Phys Lett* 2007;90:133119.
- [44] Lacour SP, Jones J, Wanger S, Li T, Suo Z. Stretchable interconnects for elastic electronic surfaces. *Proc IEEE* 2005;93:1459–67.
- [45] Song J, Huang Y, Xiao J, Wang S, Hwang KC, Ko HC, Kim DH, Stoykovich MP, Rogers J. Mechanics of noncoplanar mesh design for stretchable electronics. *J Appl Phys* 2009;105:123516.
- [46] Chen C, Tao W, Liu ZJ, Zhang YW, Song J. Controlled buckling of thin film on elastomeric substrate in large deformation. *Theor Appl Mech Lett* 2011;1:021001.
- [47] Li R, Li M, Su Y, Song J, Ni X. An analytical mechanics model for the island-bridge structures of stretchable electronics. *Soft Matter* 2013;9:8476–82.
- [48] Su Y, Wu J, Fan Z, Hwang KC, Song J, Huang Y, et al. Postbuckling analysis and its application to stretchable electronics. *J Mech Phys Solids* 2012;60:484–508.
- [49] Chen C, Tao W, Su Y, Wu J, Song J. Lateral buckling of interconnects in a non-coplanar mesh design for stretchable electronics. *ASME J Appl Mech* 2013;80:041031.
- [50] Widlund T, Yang S, Hsu Y, Lu N. Stretchability and compliance of freestanding serpentine-shaped ribbons. *Int J Solids Struct* 2014;51:4026–37.
- [51] Song J, Jiang H, Choi WM, Khang DY, Huang Y, Rogers JA. An analytical study of two-dimensional buckling of thin films on compliant substrates. *J Appl Phys* 2008;103:014303.